










## RESEARCH ARTICLE

# Dissolution of WO<sub>3</sub> modified with IrO<sub>x</sub> overlayers during photoelectrochemical water splitting

Ken J. Jenewein<sup>1,2</sup>  | Julius Knöppel<sup>1,2</sup>  | André Hofer<sup>3</sup> | Attila Kormányos<sup>1,4</sup>  |  
 Britta Mayerhöfer<sup>1,2</sup>  | Florian D. Speck<sup>1,2</sup>  | Markus Bierling<sup>1,2</sup>  |  
 Simon Thiele<sup>1,2</sup>  | Julien Bachmann<sup>3,4</sup>  | Serhiy Cherevko<sup>1</sup> 

<sup>1</sup>Helmholtz Institute Erlangen-Nürnberg for Renewable Energy (IEK-11), Forschungszentrum Jülich GmbH, Erlangen, Germany

<sup>2</sup>Department of Chemical and Biological Engineering, Friedrich-Alexander-Universität Erlangen-Nürnberg, Erlangen, Germany

<sup>3</sup>Chemistry of Thin Film Materials, Department of Chemistry and Pharmacy, Friedrich-Alexander-Universität Erlangen-Nürnberg, Erlangen, Germany

<sup>4</sup>Department of Physical Chemistry and Materials Science, Interdisciplinary Excellence Centre, University of Szeged, Szeged, Hungary

## Correspondence

Ken J. Jenewein and Serhiy Cherevko, Helmholtz Institute Erlangen-Nürnberg for Renewable Energy (IEK-11), Forschungszentrum Jülich GmbH, Cauerstrasse 1, 91058 Erlangen, Germany. Email: [k.jenewein@fz-juelich.de](mailto:k.jenewein@fz-juelich.de) and [s.cherevko@fz-juelich.de](mailto:s.cherevko@fz-juelich.de)

## Funding information

German Ministry of Education and Research (BMBF), Grant/Award Number: 03SF0564A; Deutsche Forschungsgemeinschaft (DFG), Grant/Award Number: 429730598

## Abstract

WO<sub>3</sub>, an abundant transition metal semiconductor, is one of the most discussed materials to be used as a photoanode in photoelectrochemical water-splitting devices. The photoelectrochemical properties, such as photoactivity and selectivity of WO<sub>3</sub> in different electrolytes, are already well understood. However, the understanding of stability, one of the most important properties for utilization in a commercial device, is still in the early stages. In this work, a photoelectrochemical scanning flow cell coupled to an inductively coupled plasma mass spectrometer is applied to determine the influence of co-catalyst overlayers on photoanode stability. Spray-coated WO<sub>3</sub> photoanodes are used as a model system. Iridium is applied to the electrodes by atomic layer deposition in controlled layer thickness, as determined by ellipsometry and x-ray photoelectron spectroscopy. Photoactivity of the iridium-modified WO<sub>3</sub> photoanodes decreases with increasing iridium layer thickness. Partial blocking of the WO<sub>3</sub> surface by iridium is proposed as the main cause of the decreased photoelectrochemical performance. On the other hand, the stability of WO<sub>3</sub> is notably increased even in the presence of the thinnest investigated iridium overlayer. Based on our findings, we provide a set of strategies to synthesize nanocomposite photoelectrodes simultaneously possessing high photoelectrochemical activity and photostability.

## KEYWORDS

dissolution, in situ ICP-MS, overlayers, PEC-SFC, photoelectrochemistry

## 1 | INTRODUCTION

To fight the progressing climate change, the utilization of renewable energies has to increase. Solar energy is seemingly inexhaustible and has the highest potential to

help transition into a renewable energy society. A mere 0.3% coverage of the earth's landmass with solar cells with an efficiency of 10% would satisfy the need for energy of the world's growing population.<sup>1-4</sup> The usage of solar energy, however, breeds new problems as well

This is an open access article under the terms of the [Creative Commons Attribution](https://creativecommons.org/licenses/by/4.0/) License, which permits use, distribution and reproduction in any medium, provided the original work is properly cited.

© 2023 The Authors. *SusMat* published by Sichuan University and John Wiley & Sons Australia, Ltd.

as it is intermittent. This makes it impossible to provide the baseload of electrical energy, and coupling to the electrical grid and limited storage capacities hinder an application in the transport sector. Thus, efficient solutions for energy storage and transportation have to be engaged. Solar fuels from photoelectrochemical (PEC) devices are a promising approach to overcome these limitations. The electrical energy produced from sunlight can be utilized for electrocatalytic processes, such as electrochemical water splitting, producing hydrogen, or CO<sub>2</sub> reduction to produce synthetic carbonized fuels.<sup>2,5–10</sup> These devices have made substantial progress in the recent years, showing increasing efficiency,<sup>11,12</sup> where functional devices of up to 200 cm<sup>2</sup> active area have been presented.<sup>13–15</sup>

A PEC device should provide operational stability for several years to be cost-efficient.<sup>16</sup> This requirement still hinders the fast market penetration of PEC devices as only lifetimes of up to several hundred hours have been demonstrated in laboratory settings so far.<sup>12,17</sup> A purely thermodynamic viewpoint dominates the general perception of stability in the photoelectrochemistry community. A typical n-type semiconductor is considered stable when the decomposition potential is below its valence band edge. On the contrary, the semiconductor will decompose if its decomposition potential lies above the water-splitting potential. Generally, a semiconductor is stable when the potential to decompose lies between the valence band edge and the thermodynamic potential of water splitting.<sup>18</sup> However, kinetic effects cannot be ignored. In the latter case, kinetic competition between water oxidation and photoelectrode decomposition occurs.<sup>19</sup> In fact, perceivably stable photoanodes such as WO<sub>3</sub> and BiVO<sub>4</sub> have been proven to be unstable by recently developed operando techniques, such as the PEC scanning flow coupled to an inductively coupled plasma mass spectrometer (PEC-ICP-MS).<sup>20–23</sup>

Coating the surface of the photoelectrode with a protective overlayer is a commonly applied mitigation strategy when facing severe photodegradation. The additional layers provide spatial shielding from the electrolyte and can prevent changes in the reaction kinetics at the photoelectrode surface. Two types of overlayers with different functionalities can be distinguished. First, a thin passivating oxide such as TiO<sub>2</sub> can serve as a tunneling layer. In here, the photoabsorber is shielded from the contact with the electrolyte, whereas the produced electrons can tunnel through the TiO<sub>2</sub> thin film.<sup>24–28</sup> Second, the photoanode can be decorated with oxygen evolution reaction (OER) catalysts like Co, Ir, or Ru.<sup>29–32</sup> These co-catalysts protect the photoelectrode from the electrolyte and create additional reaction sites that shift the reaction kinetics at the surface. For example, Co decoration of WO<sub>3</sub> photoanodes significantly enhanced their photoactivity and photostabil-

ity in near-neutral pH where WO<sub>3</sub> is thermodynamically unstable.<sup>29,33</sup> The deposition of RuO<sub>2</sub> nanoparticles or Ir dinuclear catalysts on WO<sub>3</sub> was shown to significantly enhanced the activity in an acidic electrolyte.<sup>32,34</sup> Co-, Ru-, and Ir-based co-catalysts can further shift the selectivity of WO<sub>3</sub> toward OER in sulfate-containing electrolytes, where instead, WO<sub>3</sub> would preferentially decompose the electrolyte to peroxide or persulfate when no co-catalyst is present.<sup>29,32,34–36</sup>

Reaction kinetics also strongly affect the photostability of WO<sub>3</sub>. As recently shown by our group, a shift from electrolyte decomposition to other reactions influences the stability of WO<sub>3</sub> photoanodes.<sup>21</sup> WO<sub>3</sub> photoanodes show a three to four-fold enhancement of photostability in HNO<sub>3</sub> and HClO<sub>4</sub> compared to H<sub>2</sub>SO<sub>4</sub> and CH<sub>3</sub>O<sub>3</sub>SH. Electrolyte decomposition involving stable reaction intermediates rather than OER in sulfur-containing electrolytes was identified as the primary contributor to these differences. These shifts were correlated to different electrolyte decomposition mechanisms.

In this work, the influence on photostability brought by the deposition of a co-catalyst on WO<sub>3</sub> photoanodes was studied. WO<sub>3</sub> model thin films were spray-coated onto fluorine-doped tin oxide (FTO) substrates based on a previously established protocol.<sup>21</sup> Then, the photoanode surface was modified with iridium layers with different thicknesses using atomic layer deposition (ALD). A previously established PEC-ICP-MS system was employed to characterize the photoactivity and in situ photostability by recording the amount of dissolved metal ions.<sup>37</sup> The photoactivity drops continuously with increasing iridium layer thickness, which hinders the light from reaching the photoabsorber during the front-illumination. However, the photostability is significantly enhanced when applying an iridium overlay, manifesting in the lowered WO<sub>3</sub> dissolution.

## 2 | METHODS

### 2.1 | Sample preparation

#### 2.1.1 | WO<sub>3</sub> photoelectrode preparation

WO<sub>3</sub> photoelectrodes were synthesized via spray-coating with an Exactacoat device (SonoTek). The precursor was prepared by dissolving 5 g tungsten powder (fine powder 99+, Merck) in 25 ml H<sub>2</sub>O<sub>2</sub> (30%, Merck).<sup>38–40</sup> After the total dissolution of tungsten powder, the solution was thermally reduced to 20 ml and diluted with IPA to 200 ml. The precleaned (10 min sonication in 2% Hellmanex III solution, 10 min sonication in DI water, and 10 min sonication in IPA) FTO glass slides (Sigma Aldrich) were placed on

an 80°C hot plate. The precursor was sprayed with a flow rate of 0.33 ml min<sup>-1</sup> at an ultrasonication power of 5 W, a nozzle height of 37 mm, and a traverse speed of 140 mm s<sup>-1</sup> in a meander-shaped pattern with a 1.5 mm pitch size.

### 2.1.2 | Iridium atomic layer deposition

The iridium film was deposited using a commercial Gemstar-6 ALD reactor from Arradiance. Ethylcyclopentadienyl-1,3-cyclohexadiene-iridium(I) ([EtCp]Ir[CHD], abcr) heated to 90°C and ozone, generated by an ozone generator model BMT 803N, were used as precursors, whereas the reaction chamber was maintained at 220°C.

## 2.2 | Characterization

**XPS:** The surface composition of the Ir-covered W samples was investigated using x-ray photoelectron spectroscopy (XPS). XPS spectra were recorded on a PHI Quantera II scanning x-ray microprobe. An Al K<sub>α</sub> irradiation with a spot diameter of 200 μm at 50 W and 15 kV with a dwell time of 200 ms per step was used. The information depth of the XPS was 5 nm. Survey scans were gathered at a step size of 0.5 and 280 eV pass energy, while high-resolution narrow scans were recorded with 0.125 eV step size at 140 eV pass energy. All spectra were evaluated in CasaXPS (v.2.3.18), applying instrument-specific relative sensitivity factors and a binding energy scale calibrated to the adventitious carbon peak at 284.8 eV.

**Ellipsometry:** The thickness of the deposited iridium thin films was determined on native Si/SiO<sub>2</sub> wafers by spectroscopic ellipsometry with a SENPro from SENTECH. The measurement was performed in a wavelength region starting at 370 nm up to 1050 nm, with a constant angle of incidence of 70°. The obtained data were fitted by the program SpectraRay/3 using an optical model, which contained the layer's thickness as well as optical constants (refraction index, psi, and delta).

**UV-vis:** Optical absorption spectra were measured with an ultraviolet-visible (UV-vis) spectrophotometer (OceanOptics) equipped with a deuterium-halogen light source (DH-2000-L) and an HR40000 spectrometer. The absorption spectra were obtained by subtracting the transmitted intensities from the incident intensity.

**XRD:** The crystal structure was analyzed by x-ray diffraction (XRD) in Bragg–Brentano geometry using a Bruker D8 Advance equipped with a Cu K<sub>α</sub> source and LynxEye XE detector.

**SEM-EDX:** The chemical composition analysis of the iridium-coated WO<sub>3</sub> photoanodes was performed with a

Zeiss Crossbeam 540 FIB-SEM with an energy dispersive detector (X-Max 150 silicon drift detector, Oxford Instruments; Software: Aztec Version 3.3, Oxford Instruments). Samples were attached with a double-sided conductive carbon tape to a secondary electron microscopy (SEM) stub. The energy-dispersive x-ray spectroscopy (EDX) was performed at a voltage of 20 kV and a probe current of 750 pA to determine the spectrum of the desired area.

**PEC-ICP-MS measurements:** In situ ICP-MS measurements were performed with a homemade PEC scanning flow cell coupled to an inductively coupled plasma mass spectrometer (Perkin Elmer NexION 350X).<sup>37</sup> The samples were placed on an XYZ-stage, which were then contacted by the cell opening with an area of 0.059 cm<sup>2</sup>. All measurements were conducted in Ar-purged 0.1 M HClO<sub>4</sub> (pH 1.67). A graphite rod (HTW) and an Ag/AgCl reference electrode (Metrohm) served as counter and reference electrodes, respectively. A metal wire was used to establish electrical contact to the sample. (Photo)electrochemical measurements were performed with a Gamry REF 600 potentiostat. The setup was controlled by a homemade LabView software. The light produced from a 300 W ozone-free Xe lamp (Newport) was passed through an AM 1.5 G filter before channeling the illumination through a liquid light guide to the working electrode. The light was calibrated to 1 Sun (100 mW cm<sup>-2</sup>) using a reference solar cell (Newport). Calibration standards were mixed freshly in 0.1 M HClO<sub>4</sub> (Merck Suprapur, diluted with deionized water, Merck Milli-Q) every day to perform a four-point calibration for Ir and W with (0, 0.5, 1, 5) μg L<sup>-1</sup>. The internal standard was 10 μg L<sup>-1</sup> Re in 0.1 M HClO<sub>4</sub>.

## 3 | RESULTS AND DISCUSSION

### 3.1 | Synthesis and characterization

The synthesis and characterization of the WO<sub>3</sub> thin films were described in our previous work.<sup>21</sup> Briefly, WO<sub>3</sub> thin films were synthesized by spray-coating a peroxotungstic acid precursor on glass slides coated with conductive FTO (for details, see experimental section). Measurements of the crystal structure by XRD after synthesis were consistent with WO<sub>3</sub> crystal structures from the crystallography open database.<sup>21,41</sup> The band gap of the thin films was determined by Tauc analysis to be 2.65 eV, which is in line with literature data.<sup>42–45</sup> SEM measurements show a fine porous structure with a layer thickness of 2–3 μm.<sup>21</sup>

The WO<sub>3</sub> thin films were coated with thin iridium layers by ALD. The WO<sub>3</sub> photoelectrodes appear less transparent after the deposition process (see Figure S1). UV-vis measurements experimentally corroborated the decreased transparency. A noncharacteristic increase in absorbance

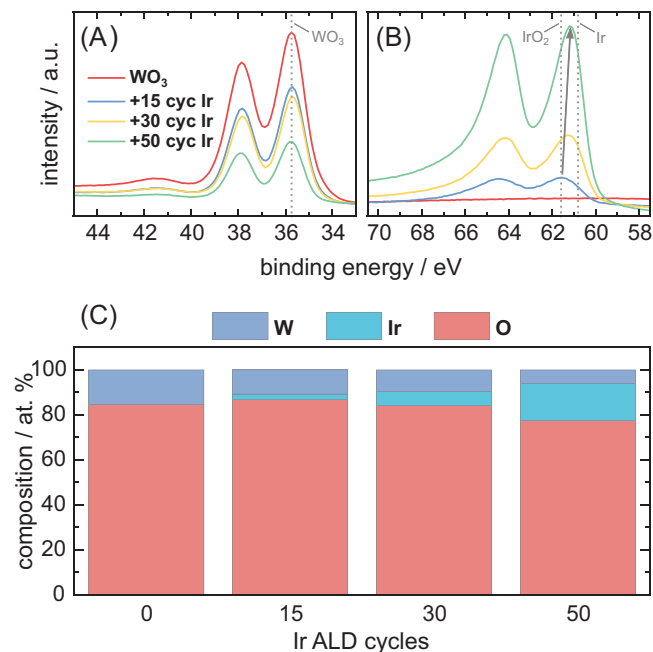


**FIGURE 1** High-resolution W4f (A) and Ir4f (B) spectra of the four WO<sub>3</sub> samples covered with various amounts of iridium. The color code shows the number of iridium atomic layer deposition (ALD) cycles. (C) Surface composition of bare WO<sub>3</sub> and WO<sub>3</sub> covered with different Ir ALD cycles determined from the survey scan

can be attributed to the iridium layer, which ultimately blocks the incident light (see Figure S2). Marginal qualitative changes between the different samples originate from the presence of scratches at the backside of the FTO substrate. SEM micrographs, as shown in Figure S3, indicate a morphologically homogeneous coating of the iridium overlayer on the pristine WO<sub>3</sub> sample. XRD spectra of iridium-decorated WO<sub>3</sub> photoanodes (see Figure S4) do not display detectable change from the pristine sample, indicating that the deposition of iridium does not alter the crystal structure of the photoabsorber.

The thickness of iridium was determined indirectly by depositing the same iridium ALD cycles on Si wafers and successively performing ellipsometry. The high surface roughness of WO<sub>3</sub> would impede any precise direct measurements of the Ir layer thickness. Previous work has demonstrated that nucleation inhibition might cause the deposited thickness of noble metals in highly porous systems to be significantly lower than its nominal value recorded on a planar reference sample suggests.<sup>46</sup> The ellipsometry measurements determined the thickness of iridium layers after 15, 30, and 50 cycles to be 0.5, 1.1, and 2.2 nm, respectively. As elemental quantification of iridium was not possible by EDX (see Figure S3), XPS analysis was performed instead. The recorded W4f peaks for all samples can be seen in Figure 1A. The binding energy of

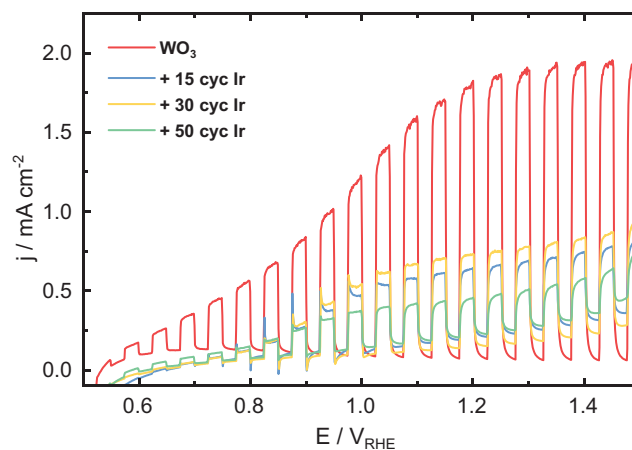


**FIGURE 2** Photovoltammograms (0.2 Hz, 1 Sun, AM 1.5 G) of WO<sub>3</sub> thin films covered with iridium layers deposited by atomic layer deposition with 5 mV s<sup>-1</sup> scan rate in 0.1 M HClO<sub>4</sub>

W4f<sub>1/2</sub> is located at 35.7 eV, with a binding energy difference of 2.1 eV characterizing the peak splitting of W4f<sub>5/2</sub>.<sup>47</sup> WO<sub>3</sub> with the thinnest iridium ALD overlayer indicates a peak at 61.6 eV, which suggests that iridium is mostly in an IrO<sub>2</sub> form (see Figure 1B). Thicker overlayers seem less oxidized, as metallic iridium is expected at 60.6 eV.<sup>48</sup> Previous reports have proposed that the oxide form is encountered for thinner iridium layers deposited by ALD. In contrast, thicker films tend to be reduced.<sup>49,50</sup> Figure 1C presents the atomic composition, which coincides with the intensities obtained from the high-resolution XPS spectra. The iridium content gradually increases at the surface as more ALD cycles are applied, reflecting a growth in the iridium film thickness. Tungsten and oxygen, on the other hand, become less abundant on the surface.

### 3.2 | Photoelectrochemical behavior

To evaluate the PEC behavior of the iridium-coated WO<sub>3</sub> films, a chopped linear sweep voltammetry (LSV) with a scan rate of 5 mV s<sup>-1</sup> and a chopping frequency of 0.2 Hz was performed in 0.1 M HClO<sub>4</sub> (pH 1.67). This electrolyte was intentionally chosen as hydrated non-specifically adsorbed ClO<sub>4</sub><sup>-</sup> anions assure minimal influence on the PEC reaction. HClO<sub>4</sub> is also routinely used to evaluate the stability of IrO<sub>x</sub> during dark OER. Thus the Ir overlayer degradation can be directly compared to the Ir dissolution behavior known for polymer electrolyte membrane water electrolyzer applications.<sup>51</sup> A 300 W Xe lamp equipped with an AM 1.5 G filter served as an illumination source and was calibrated to 1 Sun (100 mW cm<sup>-2</sup>) using a reference solar cell.

As it is shown in Figure 2, the pristine WO<sub>3</sub> film initially shows higher dark currents compared to the

co-catalyst-decorated samples. Once elevated potentials are applied, the iridium-decorated  $\text{WO}_3$  films exhibit higher dark currents. This observation can be traced back to the electrochromic redox response of  $\text{H}_x\text{WO}_3/\text{WO}_3$  around  $0.5 V_{\text{RHE}}$ .<sup>52,53</sup> As OER starts above  $1.23 V_{\text{RHE}}$ , a combination of iridium electro-oxidation and OER onset potential may be responsible for the observed higher dark current. The influence of iridium on the dark electrochemical behavior was studied further with cyclic voltammetry (CV). The CVs shown in Figure S5 indicate a pronounced Ir(IV) to Ir(III) electroreduction peak.<sup>54</sup> Similar observations regarding the dark electrochemical response were made for Ru-decorated  $\text{WO}_3$  photoelectrodes.<sup>32</sup>

The pristine  $\text{WO}_3$  thin film shows limiting photocurrents of around  $2 \text{ mA cm}^{-2}$ , which is in line with past literature.<sup>55</sup> The limiting photocurrent drops to around  $0.8 \text{ mA cm}^{-2}$  for  $\text{WO}_3$  coated with 15 and 30 iridium ALD cycles. This trend worsens further for samples with 50 ALD cycles of iridium, where the limiting photocurrent reaches only around  $0.6 \text{ mA cm}^{-2}$ . The parasitic light absorption posed by increasing layer thicknesses of iridium results in the reduction of produced charge carriers in the photoanode, lowering the photoelectrocatalytic OER. Additionally, as the overlayer thickness increases, the iridium/ $\text{WO}_3$  junction starts to prevail rather than the electrolyte/ $\text{WO}_3$ , changing the barrier height for undergoing PEC reactions, which can lead to reduced photoresponses. A similar observation was made for iridium-coated  $\text{WO}_3$  electrodes studied under front and backlight illumination.<sup>35</sup> A different behavior was shown for  $\text{RuO}_2$ -decorated  $\text{WO}_3$  surfaces. Ru had a beneficial effect on the activity of  $\text{WO}_3$  photoelectrodes.<sup>32</sup> However,  $\text{RuO}_2$  was present on the surface of  $\text{WO}_3$  as nanoparticles with a sizeable distance between each. In contrast, even the least amount of ALD cycles used in this study resulted in a thin coating partially blocking the incident light from hitting the  $\text{WO}_3$  surface. Additionally, it is hypothesized that the enhancement in PEC performance by  $\text{RuO}_2$  compared to Ir can be brought by its superior electrocatalytic activity toward OER.<sup>56</sup>

The limitation originating from light blockage was recently overcome by using iridium dinuclear heterogeneous catalysts bound to the surface of the photoelectrode.<sup>34</sup> The decoration of heterogeneous catalysts provides a synergy between negligible blockage of the light path and increased reaction rates. Additionally, it was found that the selectivity shifts from electrolyte decomposition to OER when employing sulfate-containing electrolytes. Such a major shift in product selectivity is less expected in the present study, as  $\text{HClO}_4$  is used for all PEC measurements.  $\text{WO}_3$  can decompose  $\text{ClO}_4^-$  ions to radicals, but the faradaic efficiency for  $\text{O}_2$  evolution is almost unity. In contrast, OER in  $\text{H}_2\text{SO}_4$  or  $\text{CH}_3\text{O}_3\text{SH}$  is strongly suppressed due to the favored oxidation of the

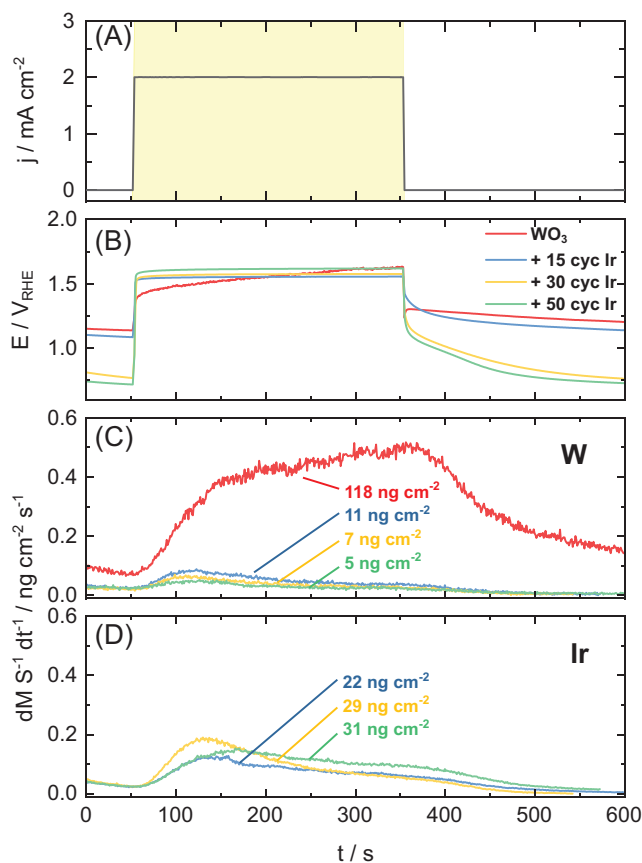


**FIGURE 3** Photoelectrochemical (PEC) measurement and dissolution profiles at a constant current step of  $2 \text{ mA cm}^{-2}$  under continuous illumination at 1 Sun AM 1.5 G. (A) Applied current density protocol with illumination indicated in yellow. (B) Measured potential. (C) Tungsten dissolution. (D) Iridium dissolution

acid anions.<sup>36,57</sup> As reaction kinetics of photoelectrodes change significantly with the application of co-catalysts, the stability of the modified photoelectrodes is most likely affected.

### 3.3 | Photoelectrochemical stability

The in situ photostability of iridium-decorated  $\text{WO}_3$  samples was recorded via a previously established PEC-ICP-MS system.<sup>37</sup> Iridium dissolution depends on the charge transferred during OER.<sup>51</sup> To ensure comparability between all samples, a chronopotentiometric protocol at  $2 \text{ mA cm}^{-2}$  was employed. Figure 3 shows the applied galvanostatic protocol, potential response, tungsten dissolution, and iridium dissolution as a function of time. As it can be seen in Figure 3B, the operating potential is reduced for the pristine  $\text{WO}_3$  sample at the beginning. However, as the current density of  $2 \text{ mA cm}^{-2}$  is kept longer, the overpotential of the pristine  $\text{WO}_3$  approaches the ones from the coated samples. This observation is indicative of

a continuous deactivation of the  $\text{WO}_3$  over time. When comparing the real-time tungsten dissolution rate recorded for all samples, it is apparent that the highest dissolution is recorded for the uncoated  $\text{WO}_3$  (see Figure 3C). While dissolution for the pristine sample peaks at around  $0.5 \text{ ng s}^{-1} \text{ cm}^{-2}$ , W dissolution rates of the Ir-coated samples stay below  $0.1 \text{ ng s}^{-1} \text{ cm}^{-2}$ . This is also apparent by comparing the total dissolved amount of W by calculating the integral of the dissolution peak. Pristine  $\text{WO}_3$  loses  $118 \text{ ng cm}^{-2}$  of W in total, whereas 11, 7, and  $5 \text{ ng cm}^{-2}$  of W are lost for the iridium-coated samples with 15, 30, and 50 ALD cycles, respectively. Assuming a  $2 \mu\text{m}$  thick  $\text{WO}_3$  layer, this roughly translates into a full dissolution of the bare  $\text{WO}_3$  after 60 h, whereas the entire loss of  $\text{WO}_3$  for the iridium-coated samples would be encountered after 640 h for the thinnest and 1408 h for the thickest iridium layer. Hence, decorating the  $\text{WO}_3$  photoelectrode, even with the thinnest iridium overlayer, dramatically suppresses W dissolution. The thin film acts as a separator that prevents the electrolyte from contacting  $\text{WO}_3$ . Moreover, the dissolution rate for the pristine  $\text{WO}_3$  increases steadily over time, coinciding with the gradual rise in overpotential (see Figure 3B) and supporting the idea of a continuous destabilization, as mentioned before. The W dissolution rate of Ir-coated samples, on the contrary, peaks at the beginning and tail-off over the course of the  $2 \text{ mA cm}^{-2}$  hold. Thus, the sudden increase in reaction rate (i.e., current density) at the beginning is more detrimental to the photoelectrode than the actual OER operation under steady-state conditions.

The iridium-coated samples show a similar iridium dissolution behavior (see Figure 3D). The dissolution rate peaks initially and decreases over time. Notably, iridium dissolution for the  $\text{WO}_3$  with 50 ALD cycles tails off slower than the other coated samples, which could be originating from the larger available quantity of iridium at the surface and its tendential metallic nature compared to 15 and 30 ALD cycles.<sup>58</sup> This higher iridium dissolution toward the end of the OER holds results in  $31 \text{ ng cm}^{-2}$  iridium being lost. An iridium loss of 22 and  $29 \text{ ng cm}^{-2}$  is recorded for 15 and 30 ALD cycles, respectively. The earlier XPS measurements, showing that thinner iridium layers are more oxidized, support this stabilization. Iridium-based electrocatalysts are typically more stable at a higher oxidation state in OER electrocatalysis.<sup>51</sup>

Similar trends were also observed when studying the in situ photostability under chronoamperometric conditions at  $1.6 \text{ V}_{\text{RHE}}$  under dark and illuminated state (see Figure S6) for bare  $\text{WO}_3$  and a representative  $\text{WO}_3$  sample coated with 50 cycles of Ir ALD. The selected potential is close to the one measured during the chronopotentiometric measurements in the study. Additionally, bare  $\text{WO}_3$  destabilizes more under illumination compared to the dark

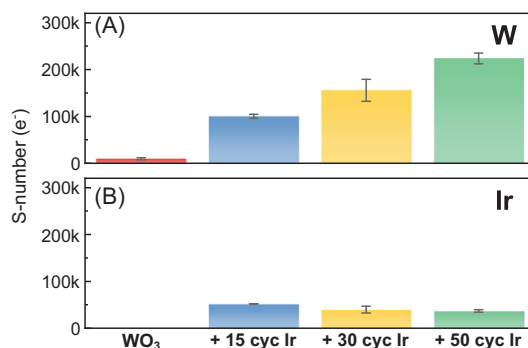


FIGURE 4 S-numbers ( $e^-$ ) for  $\text{WO}_3$  thin films covered with iridium layers from atomic layer deposition (ALD). (A) S-number ( $e^-$ ) calculated for W. (B) S-number ( $e^-$ ) calculated for Ir.

CA hold, which is expected due to the additional charge carrier generation that can cause self-oxidation of the photoanode. It appears that Ir dissolution shows a similar trend for the Ir-coated  $\text{WO}_3$  sample. While further investigations are needed to fully understand this observation, it is anticipated that holes generated at the photoanode are more efficiently transported away from the  $\text{WO}_3$  when in junction with the Ir overlayer. With the holes accumulating at the Ir co-catalyst, the probability of Ir dissolution increases in this highly oxidative environment.

The results show that iridium overlayers can effectively stabilize  $\text{WO}_3$  photoanodes but with a simultaneous sacrifice of the photoactivity. However, further considerations beyond photoactivity must be considered when using iridium in a hypothetical commercial device. Iridium is typically used as an anode catalyst in polymer electrolyte membrane water electrolyzers (PEMWE).<sup>59</sup> Thus, the utilization of iridium as co-catalyst in upscaled PEC devices has to compete against its use case in PEMWE. This necessitates drawing a valid comparison of iridium operational stability in PEMWE versus PEC water splitting. The S-number was recently introduced to enable such comparisons, which is a metric to compare the stability of iridium-based OER catalysts.<sup>51</sup> The amount of oxygen produced in the reaction is calculated from the current with an estimated faradaic efficiency of 100% toward OER and divided by the amount of dissolved catalyst material. However, the estimated faradaic efficiency of 100% toward OER is illusive for the pristine  $\text{WO}_3$ , as discussed above. Thus, the S number was slightly redefined as the fraction of the number of transferred electrons ( $e^-$ ) divided by the number of dissolved metallic catalyst (M).<sup>21</sup>

$$\text{S-number } (e^-) = \frac{n(e^-)}{n(M)} \quad (1)$$

Figure 4 shows the calculated S-numbers for both metals (W, Ir) in all samples. Before diving deeper into the

*S*-number discussion, it is necessary to justify the separate calculation for both metals, as *S* numbers are originally derived for OER catalysts with one active component. The *S*-numbers range from 25 000 to 200 000 for tungsten and are centered around 50 000 for iridium. Such high *S*-numbers indicate that only a minimal fraction of the observed current originates from the individual dissolution processes. Thus, treating iridium and tungsten dissolution as independent side reactions to the dominating OER at the electrode surface is justified. It is important to note that the *S*-number( $e^-$ ) must be divided by 4 to allow a comparison to the *S*-numbers calculated in literature for iridium electrocatalysis [ $S\text{-number} = n(\text{O}_2)/n(\text{Ir})$ ]. The *S*-numbers ( $e^-$ ) of iridium-coated  $\text{WO}_3$  range from 35 000 to 53 000, corresponding to *S*-numbers of 8750–13 250 in the iridium electrocatalysis literature.<sup>51</sup> The *S*-number of iridium correlates positively with its oxidation state. *S*-numbers between  $10^4$  and  $10^5$  can be expected for hydrous iridium oxide, whereas the *S*-number for rutile iridium oxide can even reach up to  $10^7$ .<sup>51</sup> Iridium is even more stable if utilized in PEMWE compared to aqueous model systems under acidic electrolytes, where the *S*-number can climb up to  $10^9$ .<sup>60</sup> This is several orders of magnitude above the PEC system studied here, where iridium was used as a co-catalyst for a  $\text{WO}_3$  photoelectrode.

## 4 | CONCLUSION

In this work, we demonstrated the successful deposition of iridium ALD layers onto spray-coated  $\text{WO}_3$  photoanodes. The iridium layer thickness was derived by ellipsometry, and the presence of iridium was qualitatively confirmed with XPS. The coating transitioned toward a less oxidized state with increasing iridium layer thickness. UV-vis measurements showed a noncharacteristic increase in absorbance attributed to the iridium coating blocking the incident light.

PEC measurements revealed a decrease in limiting photocurrent densities when applying more iridium layers, despite iridium being an excellent OER catalyst. The drop in photoactivity originated from the decreased charge carrier generation due to the parasitic light absorption by the iridium overlayers and a change from a predominantly electrolyte/ $\text{WO}_3$  junction to an electrolyte/iridium/ $\text{WO}_3$  junction.

The application of an overlayer has a profound impact on the stability of the photoelectrode. To reveal the in situ dissolution behavior, on-line PEC-ICP-MS measurements were performed.

Bare  $\text{WO}_3$  dissolves at a rate at which the photoelectrode would fully degrade in several hours. The deposition of even a 0.5 nm thick iridium coating visibly stabilizes

the  $\text{WO}_3$  photoanode. The stabilizing effect increases with even thicker and more dense iridium overlayers, where the coating possesses fewer defects (e.g., pinholes), which masks the photoabsorber more from contact with the electrolyte. The stabilization comes with a downside which is the similar iridium dissolution rate compared to the ones known from dark electrochemical OER. In general, even the thinnest layer of iridium (15 ALD cycles) can notably enhance the photostability of  $\text{WO}_3$ . On the other hand, this synergy comes at the cost of achievable photocurrent density, which is around 40% less compared to pristine  $\text{WO}_3$ . This performance drop is, in part, due to the light-blocking effect of the iridium overlayer and the ohmic junction present between  $\text{IrO}_2/\text{WO}_3$ . The former might be alleviated through surface decoration with single-atom catalysts, iridium nanoparticles, or dinuclear iridium catalysts.<sup>34,35,61</sup> However, their effect on the photostability of  $\text{WO}_3$  might be less pronounced, as the surface of the photoelectrode is not shielded from the electrolyte in such scenarios.

The comparison of the *S*-number calculated for iridium for different use cases (overlayer in PEC vs. PEMWE) illustrates that using iridium in PEC devices is still inferior. Nevertheless, the present work demonstrated the effectiveness of even a thin co-catalyst in enhancing the photostability. Such thin overlayers should be considered when designing new PEC systems with improved photostability. As the price of noble metals has significantly increased lately,<sup>62</sup> it is imperative to either reduce the amount of noble metals or search for non-noble alternatives that show similar stability in acidic pH.

## ACKNOWLEDGMENTS

André Hofer and Julien Bachmann thank the German Ministry of Education and Research (BMBF) and the German National Science Foundation (DFG) for financial support within the projects 03SF0564A and 429730598, respectively.


## CONFLICT OF INTEREST


The authors declare no conflict of interest.

## ORCID

Ken J. Jenewein  <https://orcid.org/0000-0001-8979-7252>

Julius Knöppel  <https://orcid.org/0000-0001-8355-3062>

Attila Kormányos  <https://orcid.org/0000-0002-2145-7419>

Britta Mayerhöfer  <https://orcid.org/0000-0002-9526-2286>

Florian D. Speck  <https://orcid.org/0000-0002-7649-9261>

Markus Bierling  <https://orcid.org/0000-0002-4992-2095>

Simon Thiele  <https://orcid.org/0000-0002-4248-2752>

Julien Bachmann  <https://orcid.org/0000-0001-6480-6212>

6212

Serhiy Cherevko  <https://orcid.org/0000-0002-7188-4857>

## REFERENCES

- Kim JH, Hansora D, Sharma P, Jang JW, Lee JS. Toward practical solar hydrogen production - an artificial photosynthetic leaf-to-farm challenge. *Chem Soc Rev*. 2019;48(7):1908-1971.
- Armaroli N, Balzani V. *Energy for a Sustainable World: From the Oil Age to a Sun-Powered Future*. Wiley-VCH; 2010:390.
- Jacobson MZ. Review of solutions to global warming, air pollution, and energy security. *Energy Environ Sci*. 2009;2(2):148-173.
- Roger I, Shipman MA, Symes MD. Earth-abundant catalysts for electrochemical and photoelectrochemical water splitting. *Nat Rev Chem*. 2017;1(1):0003.
- Ran J, Jaroniec M, Qiao SZ. Cocatalysts in semiconductor-based photocatalytic CO<sub>2</sub> reduction: achievements, challenges, and opportunities. *Adv Mater*. 2018;30(7).
- De Luna P, Hahn C, Higgins D, Jaffer SA, Jaramillo TF, Sargent EH. What would it take for renewably powered electrosynthesis to displace petrochemical processes? *Science*. 2019;364(6438):eaav3506.
- Roel Van de Krol MG. *Photoelectrochemical Hydrogen Production*. Springer US; 2012.
- Nocera DG. The artificial leaf. *Acc Chem Res*. 2012;45:767-776.
- Ardo S, Rivas DF, Modestino MA, et al. Pathways to electrochemical solar-hydrogen technologies. *Energy Environ Sci*. 2018;11(10):2768-2783.
- Grätzel M. Photoelectrochemical cells. *Nature*. 2001;414:338-344.
- Tembhurne S, Nandjou F, Haussener S. A thermally synergistic photo-electrochemical hydrogen generator operating under concentrated solar irradiation. *Nat Energy*. 2019;4(5):399-407.
- Cheng W-H, Richter MH, May MM, et al. Monolithic photoelectrochemical device for direct water splitting with 19% efficiency. *ACS Energy Lett*. 2018;3(8):1795-1800.
- Ahmet IY, Ma Y, Jang J-W, et al. Demonstration of a 50 cm<sup>2</sup> BiVO<sub>4</sub> tandem photoelectrochemical-photovoltaic water splitting device. *Sustainable Energy Fuels*. 2019;3(9):2366-2379.
- Vilanova A, Dias P, Azevedo J, et al. Solar water splitting under natural concentrated sunlight using a 200 cm<sup>2</sup> photoelectrochemical-photovoltaic device. *J Power Sources*. 2020;454:227890.
- Lee WJ, Shinde PS, Go GH, Ramasamy E. Ag grid induced photocurrent enhancement in WO<sub>3</sub> photoanodes and their scale-up performance toward photoelectrochemical H<sub>2</sub> generation. *Int J Hydrogen Energy*. 2011;36(9):5262-5270.
- Pinaud BA, Benck JD, Seitz LC, et al. Technical and economic feasibility of centralized facilities for solar hydrogen production via photocatalysis and photoelectrochemistry. *Energy Environ Sci*. 2013;6(7):1983-2002.
- Bae D, Pedersen T, Seger B, et al. Carrier-selective p- and n-contacts for efficient and stable photocatalytic water reduction. *Catal Today*. 2017;290:59-64.
- Chen S, Wang L-W. Thermodynamic oxidation and reduction potentials of photocatalytic semiconductors in aqueous solution. *Chem Mater*. 2012;24(18):3659-3666.
- Nandjou F, Haussener S. Kinetic competition between water-splitting and photocorrosion reactions in photoelectrochemical devices. *ChemSusChem*. 2019;12(9):1984-1994.
- Knöppel J, Zhang S, Speck FD, Mayrhofer KJJ, Scheu C, Cherevko S. Time-resolved analysis of dissolution phenomena in photoelectrochemistry – a case study of WO<sub>3</sub> photocorrosion. *Electrochem Commun*. 2018;96:53-56.
- Knöppel J, Kormányos A, Mayerhöfer B, et al. Photocorrosion of WO<sub>3</sub> photoanodes in different electrolytes. *ACS Phys Chem Au*. 2021;1(1):6-13.
- Zhang SY, Rohloff M, Kasian O, et al. Dissolution of BiVO<sub>4</sub> photoanodes revealed by time-resolved measurements under photoelectrochemical conditions. *J Phys Chem C*. 2019;123(38):23410-23418.
- Zhang S, Ahmet I, Kim SH, et al. Different photostability of BiVO<sub>4</sub> in near-pH-neutral electrolytes. *ACS Appl Energy Mater*. 2020;3(10):9523-9527.
- Bae D, Seger B, Vesborg PC, Hansen O, Chorkendorff I. Strategies for stable water splitting via protected photoelectrodes. *Chem Soc Rev*. 2017;46(7):1933-1954.
- Mei B, Pedersen T, Malacrida P, et al. Crystalline TiO<sub>2</sub>: a generic and effective electron-conducting protection layer for photoanodes and -cathodes. *J Phys Chem C*. 2015;119(27):15019-15027.
- Tang-Kong R, Winter R, Brock R, et al. The role of catalyst adhesion in ALD-TiO<sub>2</sub> protection of water splitting silicon anodes. *ACS Appl Mater Interfaces*. 2018;10(43):37103-37109.
- Scheuermann AG, Prange JD, Gunji M, Chidsey CED, McIntyre PC. Effects of catalyst material and atomic layer deposited TiO<sub>2</sub> oxide thickness on the water oxidation performance of metal-insulator-silicon anodes. *Energy Environ Sci*. 2013;6(8):2487-2496.
- Papp J, Soled S, Dwight K, Wold A. Surface acidity and photocatalytic activity of TiO<sub>2</sub>, WO<sub>3</sub>/TiO<sub>2</sub>, and MoO<sub>3</sub>/TiO<sub>2</sub> photocatalysts. *Chem Mater*. 1994;6(4):496-500.
- Seabold JA, Choi K-S. Effect of a cobalt-based oxygen evolution catalyst on the stability and the selectivity of photo-oxidation reactions of a WO<sub>3</sub> photoanode. *Chem Mater*. 2011;23(5):1105-1112.
- Mei B, Seger B, Pedersen T, et al. Protection of p(+)-n-Si photoanodes by sputter-deposited Ir/IrOx thin films. *J Phys Chem Lett*. 2014;5(11):1948-1952.
- Ben-Naim M, Palm DW, Strickler AL, et al. A spin coating method to deposit iridium-based catalysts onto silicon for water oxidation photoanodes. *ACS Appl Mater Interfaces*. 2020;12(5):5901-5908.
- Janáky C, Chanmanee W, Rajeshwar K. On the substantially improved photoelectrochemical properties of nanoporous WO<sub>3</sub> through surface decoration with RuO<sub>2</sub>. *Electrocatalysis*. 2013;4(4):382-389.
- Pourbaix M. *Atlas of Electrochemical Equilibria in Aqueous Solutions*. NACE International; 1974.
- Zhao Y, Yan X, Yang KR, et al. End-on bound iridium dinuclear heterogeneous catalysts on WO<sub>3</sub> for solar water oxidation. *ACS Cent Sci*. 2018;4(9):1166-1172.
- Spurgeon JM, Velazquez JM, McDowell MT. Improving O<sub>2</sub> production of WO<sub>3</sub> photoanodes with IrO<sub>2</sub> in acidic aqueous electrolyte. *Phys Chem Chem Phys*. 2014;16(8):3623-3631.
- Mi Q, Zhanaidarova A, Brunschwig BS, Gray HB, Lewis NS. A quantitative assessment of the competition between water



- and anion oxidation at WO<sub>3</sub> photoanodes in acidic aqueous electrolytes. *Energy Environ Sci.* 2012;5(2):5694-5700.
37. Jenewein KJ, Kormányos A, Knöppel J, Mayrhofer KJJ, Cherevko S. Accessing in situ photocorrosion under realistic light conditions: photoelectrochemical scanning flow cell coupled to online ICP-MS. *ACS Measure Sci Au.* 2021;1(2):74-81.
  38. Nanba T, Takano S, Yasui I, Kudo T. Structural study of peroxopolytungstic acid prepared from metallic tungsten and hydrogen peroxide. *J Solid State Chem.* 1991;90(1):47-53.
  39. Vidmar T, Topič M, Dzik P, Opara Krašovec U. Inkjet printing of sol-gel derived tungsten oxide inks. *Sol Energy Mater Sol Cells.* 2014;125:87-95.
  40. Kwong WL, Savvides N, Sorrell CC. Electrodeposited nanostructured WO<sub>3</sub> thin films for photoelectrochemical applications. *Electrochim Acta.* 2012;75:371-380.
  41. Grazulis S, Chateigner D, Downs RT, et al. Crystallography Open Database - an open-access collection of crystal structures. *J Appl Crystallogr.* 2009;42(4):726-729.
  42. Yang B, Barnes PRF, Bertram W, Luca V. Strong photoresponse of nanostructured tungsten trioxide films prepared via a sol-gel route. *J Mater Chem.* 2007;17:2722-2729.
  43. Yang B, Zhang Y, Drabarek E, Barnes PRF, Luca V. Enhanced photoelectrochemical activity of sol-gel tungsten trioxide films through textural control. *Chem Mater.* 2007;19(23):5664-5672.
  44. Tanaka D, Oaki Y, Imai H. Enhanced photocatalytic activity of quantum-confined tungsten trioxide nanoparticles in mesoporous silica. *Chem Commun (Camb).* 2010;46(29):5286-5288.
  45. Butler MA. Photoelectrolysis and physical properties of the semiconducting electrode WO<sub>2</sub>. *J Appl Phys.* 1977;48(5):1914-1920.
  46. Schlicht S, Büttner P, Bachmann J. Highly active Ir/TiO<sub>2</sub> electrodes for the oxygen evolution reaction using atomic layer deposition on ordered porous substrates. *ACS Appl Energy Mater.* 2019;2(3):2344-2349.
  47. Fleisch TH, Mains GJ. An XPS study of the UV reduction and photochromism of MoO<sub>3</sub> and WO<sub>3</sub>. *J Chem Phys.* 1982;76(2):780-786.
  48. Kasian O, Geiger S, Schalenbach M, et al. Using instability of a non-stoichiometric mixed oxide oxygen evolution catalyst as a tool to improve its electrocatalytic performance. *Electrocatalysis.* 2017;9(2):139-145.
  49. Hämäläinen J, Ritala M, Leskelä M. Atomic layer deposition of noble metals and their oxides. *Chem Mater.* 2013;26(1):786-801.
  50. Schlicht S, Haschke S, Mikhailovskii V, Manshina A, Bachmann J. Highly reversible water oxidation at ordered nanoporous iridium electrodes based on an original atomic layer deposition. *ChemElectroChem.* 2018;5(9):1259-1264.
  51. Geiger S, Kasian O, Ledendecker M, et al. The stability number as a metric for electrocatalyst stability benchmarking. *Nat Catal.* 2018;1(7):508-515.
  52. Amano F, Tian M, Wu G, Ohtani B, Chen A. Facile preparation of platelike tungsten oxide thin film electrodes with high photoelectrode activity. *ACS Appl Mater Interfaces.* 2011;3(10):4047-4052.
  53. Cai M, Fan P, Long J, et al. Large-scale tunable 3D self-supporting WO<sub>3</sub> micro-nano architectures as direct photoanodes for efficient photoelectrochemical water splitting. *ACS Appl Mater Interfaces.* 2017;9(21):17856-17864.
  54. Pickup PG, Birss VI. A model for anodic hydrous oxide growth at iridium. *J Electroanal Chem Interfacial Electrochem.* 1987;220(1):83-100.
  55. Santato C, Ulmann M, Augustynski J. Photoelectrochemical properties of nanostructured tungsten trioxide films. *J Phys Chem B.* 2001;105(5):936-940.
  56. Cherevko S, Geiger S, Kasian O, et al. Oxygen and hydrogen evolution reactions on Ru, RuO<sub>2</sub>, Ir, and IrO<sub>2</sub> thin film electrodes in acidic and alkaline electrolytes: a comparative study on activity and stability. *Catal Today.* 2016;262:170-180.
  57. Knöppel J, Kormányos A, Mayerhöfer B, et al. Photocorrosion of WO<sub>3</sub> photoanodes in different electrolytes. *ACS Phys Chem Au.* 2021;1(1):6-13.
  58. Li T, Kasian O, Cherevko S, et al. Atomic-scale insights into surface species of electrocatalysts in three dimensions. *Nat Catal.* 2018;1(4):300-305.
  59. Carmo M, Fritz DL, Merge J, Stolten D. A comprehensive review on PEM water electrolysis. *Int J Hydrogen Energy.* 2013;38(12):4901-4934.
  60. Knöppel J, Möckl M, Escalera-Lopez D, et al. On the limitations in assessing stability of oxygen evolution catalysts using aqueous model electrochemical cells. *Nat Commun.* 2021;12(1):2231.
  61. Zhao Y, Yang KR, Wang Z, et al. Stable iridium dinuclear heterogeneous catalysts supported on metal-oxide substrate for solar water oxidation. *Proc Natl Acad Sci U S A.* 2018;115(12):2902-2907.
  62. Johnson Matthey daily prices between 01 Jul 2020 and 28 May 2021. Johnson Matthey; 2021. Accessed May 28, 2021. <http://www.platinum.matthey.com/prices/price-charts#>

## SUPPORTING INFORMATION

Additional supporting information can be found online in the Supporting Information section at the end of this article.

**How to cite this article:** Jenewein KJ, Knöppel J, Hofer A, et al. Dissolution of WO<sub>3</sub> modified with IrO<sub>x</sub> overlayers during photoelectrochemical water splitting. *SusMat.* 2023;3:128-136. <https://doi.org/10.1002/sus2.107>